Environmental Science and Pollution Research (2022) 29:49322–49334
https://doi.org/10.1007/s11356-021-18276-7

RESEARCH ARTICLE

Manganese oxide-modified biochar derived from discarded mushroom-stick for the removal of Sb(III) from aqueous solution

Wenjian Mao[1] · Pan Wu[1,2,3] · Yuqin Zhang[1] · Kaidi Lai[4] · Lisha Dong[1] · Xufeng Qian[1] · Yuntao Zhang[1] · Jian Zhu[1,2,3]

Received: 4 September 2021 / Accepted: 18 December 2021 / Published online: 26 February 2022

ABSTRACT

In this study, discarded mushroom-stick, which is widely available, was selected as a precursor to prepare MnO_2-modified biochar (MBC) for Sb(III) removal. Several characterisation methods (SEM, BET, XPS, FT-IR, and XRD) were used to explore the mechanisms of antimony adsorption onto MBC. The results showed that MBC is a mesoporous material with a fluffy structure and a higher specific surface area (23.56 and 32.09 $m^2 \cdot g^{-1}$) than PBC600 (13.62 $m^2 \cdot g^{-1}$), exhibiting superior and stable adsorption capacities for Sb(III) (50.30 $mg \cdot g^{-1}$ for 1/30MBC600 and 64·12 $mg \cdot g^{-1}$ for 1/20MBC600) across a wide pH range (pH 4–8). X-ray photoelectron spectroscopy (XPS) and Fourier transform infrared (FT-IR) spectroscopy analyses indicated that the main oxides and functional groups involved in the adsorption were manganese oxides and hydroxyl groups. Forty-four per cent of the adsorbed Sb(III) was oxidised to Sb(V) by manganese oxides or hydroxyl groups both on the surface of biochar and in solution. According to adsorption kinetics and isotherms, the adsorption process of Sb(III) is chemisorption, which includes monolayer and multilayer heterogeneous chemisorption processes. To sum up, MBC is an excellent adsorbent for the capture of Sb(III) from contaminated water with strong potential for future application.

Keywords Manganese oxide · Modify · Discarded mushroom-stick · Biochar · Antimony

Introduction

Large-scale mining activities and smelting industries using antimony (Sb)-containing products have triggered extremely serious antimony pollution (He et al. 2012). Antimony mainly exists in the aquatic environment in two oxidation states (Sb(III) and Sb(V)), with Sb(III) being more mobile and 10 more times toxic than Sb(V) (Guo et al. 2021). Antimonite ion [$Sb(OH)_6^-$] and antimony hydroxide [$Sb(OH)_3$] prevail in natural water and differ from other heavy metals which exist as cations (Herath et al. 2017). These emerging contaminants have adverse outcomes on human health and ecosystems (Luo et al. 2021). Excessive antimony exposure is extremely harmful to human beings, causing gene mutation and dysregulation of the immune and nervous systems due to the high toxicity of Sb (Li et al. 2021; Nishad and Bhaskarapillai, 2021). Currently, many researchers are developing more efficient methods to prevent Sb from entering the environment or to sequester Sb from contaminated water (Qi et al. 2021). However, the complex speciation of Sb makes it difficult to identify effective antimony removal technologies (Zhang et al. 2021b). Recently, various techniques have been proposed for Sb removal including chemical precipitation, flocculation/coagulation, membrane separation, and adsorption. Among them, multiple carbon-based material adsorbents (activated carbon, carbon nanotube, biochar, and so on) have been applied to adsorb Sb from aqueous solution (Hu et al. 2020). In particular, biochar was deemed as the most promising adsorbent attracting extensive attention because of its economic viability, efficacy, and environmental sustainability (Thomas et al. 2020).

Responsible Editor: Zhihong Xu

✉ Jian Zhu
jzhu@gzu.edu.cn

[1] Resource and Environmental Engineering College, Guizhou University, Guiyang 550025, People's Republic of China

[2] Key Laboratory of Karst Georesources and Environment (Guizhou University), Ministry of Education, Guiyang 550025, People's Republic of China

[3] Guizhou Karst Environmental Ecosystems Observation and Research Station, Ministry of Education, Guiyang 550025, People's Republic of China

[4] Guizhou Environment and Engineering Appraisal Center, Guiyang 550002, People's Republic of China

Biochar is the porous carbon-rich material of biomass produced by high-temperature pyrolysis in limited oxygen. Biochar has a porous and loose structure which results in a large specific surface area, and abundant functional groups (carboxyl, hydroxyl, carbonyl, etc.) (Pan et al. 2021). Biochar has been widely used in various fields, including soil modification, water pollution control, battery development, catalysis, and air purification (Huang et al. 2021). Biochar has also been adopted as efficient adsorbents for the removal of heavy metals from water, such as Cd, Pb, Cu, As, Sb, and Cr (Calugaru et al. 2019; Herath et al. 2021; Jin et al. 2021; Kamran and Park, 2020; Lian et al. 2020; Song et al. 2019; Zou et al. 2021). Currently, studies on the adsorption of Sb by biochar are still in relatively early stages, and the adsorption capacity of pristine biochar is usually poor. The mechanisms of the adsorption of Sb onto biochar remain unclear (Cui et al. 2017; Wei et al. 2020; Zhu et al. 2021). Given the many advantages of biochar, we proposed that there is an urgent need to design a novel modified biochar that is able to efficiently remove Sb from aqueous solution, and that this is a topic deserving considerable investment (Vithanage et al. 2015; Zhu et al. 2021).

Discarded mushroom-stick is the spent substrate that remains after the production of mushrooms (Li et al. 2020). As hyphae grow, they can penetrate the cytoderm of plant cells and decompose lignin, cellulose, and hemicellulose to obtain nutrients, leading to the formation of the loose structure of biomass (Chen et al. 2020). This is conducive to improving the surface area and activation efficiency of biochar. Therefore, discarded mushroom-stick is an excellent raw material for biochar production, as it not only repurposes waste material but also has obvious environmental and economic benefits, with China producing 80 million tons of discarded mushroom-stick each year (Cheng et al. 2019; Kumar et al. 2021). Discarded mushroom-stick is generally disposed of or burned, which not only leads to possible soil or air pollution but also misses an opportunity to recover resources (Castanho et al. 2021). Despite the immense challenges associated with recycling and reusing this discarded mushroom-stick material, significant improvements have been made in this field (Hou et al. 2021; Khan et al. 2021).

Manganese dioxide (MnO_2) has gained particular attention and has been implemented for environmental improvement over recent decades. MnO_2 has several important properties, including environmental compatibility, strong oxidising ability, adsorptive ability, acid resistance, and low cost (Yang et al. 2021). Such advantages make it a promising functional nanomaterial, which not only acts as an adsorbent material for the removal of heavy metals but also a catalyst to degrade persistent organic pollutants (He et al. 2021; Zhang et al. 2020a). Currently, many studies indicate that MnO_2 has a strong affinity to Sb and As such that it can steadily adsorb Sb and As to achieve a better removal effect (Ge et al. 2016; Li et al. 2018; Liu et al. 2020). However, a series of drawbacks limit its practical application: it presents as a fine powder, easily agglomerates, and is difficult to separate (Wang et al. 2015). Hence, there is an urgent need to develop MnO_2 composite materials that have more extensive application prospects. Specifically, the aforementioned disadvantages can be overcome by dispersing MnO_2 particles into porous materials such as biochar (Tian et al. 2021). Biochar loaded with MnO_2 has improved stability and enhanced adsorption capacity, while also achieving a much greater separation effect and adaptability (Cuong et al. 2021). Thus, MnO_2-modified biochar (MBC) is of great promise.

In this study, we fabricated three pristine biochar samples at different pyrolysis temperatures (PBC400, PBC500, and PBC600) and three MnO_2-modified biochar samples (1/20MBC, 1/30MBC, and 1/50MBC) using a chemical coprecipitation method. Two kinds of biochar samples were applied to adsorb Sb(III) in aqueous solution. The effects of pyrolysis temperature, initial Sb(III) concentration, and initial pH on Sb(III) adsorption onto the biochar samples were evaluated in batch adsorption experiments. The mechanisms of Sb(III) adsorption onto MBC were determined by Fourier transform infrared spectroscopy (FT-IR), X-ray photoelectron spectroscopy (XPS), and X-ray diffractometry (XRD).

Materials and methods

Chemicals and reagents

All reagents and chemicals were of analytical grade or better. Discarded mushroom-stick was supplied by a farm located in Huaxi District, Guiyang City, Guizhou Province. Ultrapure water (18.2 $M\Omega \cdot cm^{-1}$) was used for all the experiments. Potassium antimony tartrate ($C_8H_{10}K_2O_{15}Sb_2$) was purchased from Tianjin Kemiou Chemical Reagent Co., Ltd. Manganese sulphate monohydrate and potassium permanganate came from Chengdu Jinshan Chemical Reagent Co., Ltd and Chongqing Chuanjiang Chemical Reagent Factory, respectively. A standard Sb solution of 1.0 $g \cdot L^{-1}$ was used for the preparation of all standard calibration curves.

Preparation of PBC and MBC composites

The fabrication procedures for the pristine biochar (PBC) and MnO_2-modified biochar (MBC) composites were performed according to Fig. S1. Discarded mushroom-stick was washed with tap water several times to remove the residue, and then dried at 80 °C for 24 h. The dried discarded mushroom-stick was ground into fine powder. Then, the sample was transferred into a muffle furnace and pyrolysed at different pyrolysis temperatures (400 °C, 500 °C, and 600 °C) with a heating rate of 10 $°C \cdot min^{-1}$ for a period of 4 h. After the furnace temperature

returned to room temperature, the pyrolysed sample was collected and ground into fine powder again to pass through 100-mesh sieves. The 100-mesh sample was washed with ultrapure water several times until the pH value reached 7. The resultant biochar was dried at 80 °C for 24 h to obtain the composite and then stored in a small valve bag for further experimental use. The fabricated biochar samples were labelled as PBC400, PBC500, and PBC600 based on the temperature applied.

MBC was prepared according to a chemical co-precipitation method that has been previously published (Shen et al. 2020). 0.2332 g of $MnSO_4{\cdot}H_2O$ and 4.00 g of PBC600 were mixed in 200 mL of deionised water with slow stirring. Then, the mixed suspension underwent ultrasound for 1 h to ensure close contact of $MnSO_4$ and PBC600. Twenty millilitres of dissolved $KMnO_4$ (0.1453 g) was then gradually added to the suspension under slow stirring. The stoichiometric mole ratio of $KMnO_4$: $MnSO_4{\cdot}H_2O$ was 2: 3, and the prepared mass ratios of MnO_2 to BC were 1:20. The synthesis of MBC was based on the comproportionation reaction which took place in the solution phase as described in Eq. (1) (Gao et al. 2018):

$$2MnO_4^- + 3Mn^{2+} + 2H_2O \rightarrow 5MnO_2 \downarrow + 4H^+ \quad (1)$$

This reaction was carried out in open-air conditions for 24 h. The product was washed using ultrapure water several times and then separated, followed by drying at 80 °C for 12 h to obtain biochar powders. The fabricated biochar samples were named 1/20MBC600. The same procedures were performed to prepare 1/30MBC600 and 1/50MBC600.

Material characterisations

Field emission scanning electron microscopy was used to examine the surface morphologies and structural properties (FESEM, ZEISS Sigma500). The physicochemical properties of different biochar samples and their relationships with surface area, porosity, and pore volume were determined by a Brunauer–Emmett–Teller system (BET, ASAP2020). A Fourier transform infrared spectroscopy (FT-IR, Nicolet IS5) instrument was used to detect the functional groups on the material surface. X-ray photoelectron spectroscopy (XPS, Thermo SCIENTIFIC ESCALAB 250Xi) was used to analyse the surface composition. X-ray diffractometry (XRD, Ultima IV) was used to characterise the phase structures of the samples.

Batch sorption experiments

The 1000 $mg{\cdot}L^{-1}$ stock solution was prepared by dissolving 1000 mg potassium antimony tartrate ($C_8H_{10}K_2O_{15}Sb_2$) in 1 L ultrapure water and 100 $mg{\cdot}L^{-1}$ working solutions were prepared by dilution with ultrapure water. 100 $mg{\cdot}L^{-1}$ working solutions were used for all the experiments except for the determination of the effect of initial Sb(III) concentration. The pH of the reaction solution was adjusted with 0.1 M HCl or KOH before adding biochar to initiate all the experiments. Experiments to determine the influence of pyrolysis temperature (PBC400, PBC500, and PBC600) and MnO_2:BC mass ratio (1/20MBC600, 1/30MBC600, and 1/50MBC600) on Sb(III) adsorption were carried out in a 150 mL Erlenmeyer flask with a solution volume of 100 mL and a sample mass of 0.1 g. The effects of the initial pH and initial Sb(III) concentration on Sb(III) adsorption onto the biochar in aqueous solution were investigated under the same conditions. The batch adsorption tests were carried out using a thermostatic oscillator at 150 rpm with a constant temperature of 25 °C.

At given time intervals (0–24 h), 1 ml of sample was collected and filtered (Millipore 0.45 μm) immediately. The obtained sample was mixed with 9 ml of 0.5 M HCl for preservation at 4 °C in the dark, awaiting detection of Sb(III) and Sb(T). Sb(III) and Sb(T) were determined using hydride generation-atomic fluorescence spectrometry (HG-AFS9700, Haiguang, Beijing). The Sb(V) concentration was acquired by deducting the concentration of Sb(III) from that of Sb(T) (Costa Ferreira et al. 2019; Wang et al. 2020).

The removal efficiency of Sb (R) was calculated using Eq. (2):

$$R = \frac{\Delta C}{C_0}, \Delta C = (C_0 - C) \quad (2)$$

and the adsorption capacity q ($mg{\cdot}g^{-1}$) of Sb was calculated using Eq. (3):

$$q = \frac{\Delta C}{m} V, \Delta C = (C_0 - C) \quad (3)$$

where C_0 and C are the initial and final Sb concentrations ($mg{\cdot}L^{-1}$) in the sample solution, respectively, V is the solution volume (L), and m is the mass of the adsorbent used (g).

Adsorption kinetics and isotherm

It is crucial to gain a greater understanding of the process by which Sb(III) adsorbs onto the MBC; hence, two different adsorption kinetics models were applied to fit the data (Jin et al. 2021). The experimental conditions involved an initial pH of 4.0, an adsorbent dosage of 1 $g{\cdot}L^{-1}$, and a constant temperature of 25 °C. Samples were taken at specified time intervals (0–24 h) and analysed. The pseudo-first-order model is given in Eq. (4) (Song et al. 2019):

$$q_t = q_e\left(1 - e^{-k_1 t}\right) \quad (4)$$

The pseudo-second-order model is shown in Eq. (5) (Song et al. 2019):

$$q_t = \frac{q_e^2 k_2 t}{1 + q_e k_2 t} \tag{5}$$

where t (min) is the retention time, q_e and q_t (mg·g^{-1}) represent the amount of Sb adsorbed onto the adsorbent at equilibrium and a certain time, respectively. K_1 (min^{-1}) and K_2 (g/mg·min^{-1}) are the rate constants of the pseudo-first-order and pseudo-second-order models, respectively.

Isotherm studies were conducted to investigate the adsorption characteristics of each biochar under similar conditions as the adsorption kinetics experiments, using constant temperatures of 25 °C and 35 °C, and various initial Sb(III) concentrations (Liu et al. 2021a). The Langmuir model is derived from the hypothesis of monolayer adsorption between gas and solid phases. The Freundlich equation is a semi-empirical equation that can be used for surface adsorption and multilayer adsorption under various non-ideal conditions. The equations of the Langmuir and Freundlich models are provided as Eq. (6) and Eq. (7) (Song et al. 2019):

$$q_e = \frac{q_m b C_e}{1 + b C_e} \tag{6}$$

$$q_e = K_F C_e^n \tag{7}$$

where C_e is the concentration of Sb (mg·L^{-1}) at equilibrium, q_e is the adsorption capacity (mg·g^{-1}) and q_m is the maximum adsorption amount corresponding to monolayer adsorption (mg·g^{-1}), b (L·mg^{-1}) and K_F are the equilibrium constants, and n is the constant that represents adsorption strength.

Results and discussion

Characteristics of PBC and MBC

The major physicochemical properties of PBC600 and MBC600 are presented in Table 1. As the amount of MnO_2 increased, the elemental Mn content and BET surface area of the biochar also increased. Figure 1a shows the SEM-elemental mapping image of 1/20MBC600 and the morphological characteristics of 1/30MBC600 and PBC600 are provided in Fig. S2. The surface morphologies of the three samples were very rough and particles were small. For MBC, there was an obvious manganese element peak detected by XPS (Fig. 1b) (Wang et al. 2015). All the above analyses suggested that MBC was successfully synthesised after the chemical co-precipitation of $KMnO_4$ and $MnSO_4$. N_2 adsorption–desorption isotherms of the PBC600, 1/30MBC600, and 1/20MBC600 samples are shown in Fig. 1c, and obvious hysteresis loops were observed between the adsorption and desorption curves at nearly $P/P_0 > 0.45$ for all the samples, indicating the presence of mesopores (Cuong et al. 2021). Figure 1d presents pore size distribution plots of these three samples mentioned above. The dominating distribution was in the range of 2–100 nm for all the samples, further suggesting that they were mesoporous materials (Yao et al. 2020). Generally, mesopores play a critical role in diffusion, which is important for improving the efficiency of Sb removal(Hou et al. 2021).

Batch sorption experiments

Effect of different pyrolysis temperatures of biochar samples on Sb(III) adsorption

The pyrolysis temperature has a vital impact on the heavy metal adsorption behaviour of the biochar as it greatly affects its physicochemical properties (Hu et al. 2020). Therefore, it is of great importance to explore the influence of different pyrolysis temperatures on Sb(III) adsorption. As mentioned in **Sect. 2.4**, PBC400, PBC500, and PBC600 were applied to carry out adsorption experiments. As shown in Fig. 2a, among the three biochar samples, PBC600 performed best in terms of Sb(III) removal, with adsorption capacity reaching 3.86 mg·g^{-1}, followed by PBC500 (1.99 mg·g^{-1}) and PBC400 (1.80 mg·g^{-1}). Generally, the BET specific surface area and total pore volume of biochar increased significantly as the pyrolysis temperature was increased, both of which led to a higher capacity to remove heavy metal ions (Leng et al. 2021); this is consistent with Table 1. Other studies have confirmed that increased surface precipitation and ion exchange properties promote the adsorption of heavy metals such as Cu and Cr(VI) by high-temperature biochar (Jin et al. 2021; Song et al. 2019). However, previous studies also demonstrated that a lower pyrolysis temperature can contribute to more

Table 1 Major physicochemical properties of PBC600, 1/30MBC600, and 1/20MBC600

Sample	S_{BET}(m^2.g^{-1})	Average pore diameter(μm)	V_{tot}(cm^3.g^{-1})	Surface atom composition(m%)				
				C	N	O	S	Mn
PBC600	13.62	20.05	0.067	57.07	3.78	36.71	2.44	--
1/30MBC600	23.56	13.11	0.076	80.75	5.72	10.80	1.73	1.01
1/20MBC600	32.09	13.30	0.075	62.24	2.90	25.62	1.79	7.45

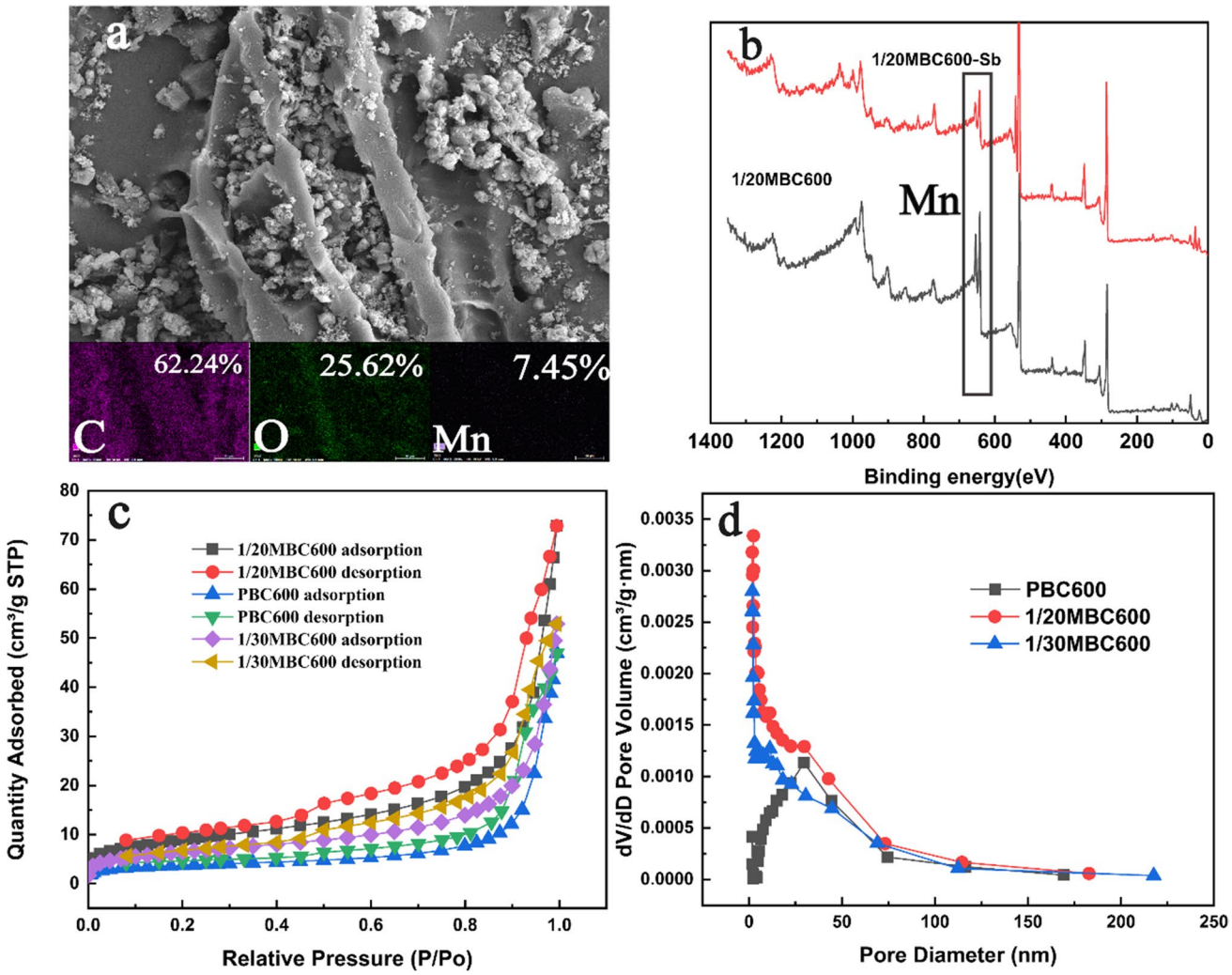

Fig. 1 FESEM image and elemental mapping of (**a**) 1/20MBC600, XPS patterns of the 1/20MBC600 and 1/20MBC600-Sb(**b**), (**c**) Nitrogen adsorption/desorption isotherms and (**d**) BJH pore size distributions of PBC600, 1/30MBC600, and 1/20MBC600

abundant functional groups in the biochar, which is beneficial for Sb(III) adsorption (Cui et al. 2017). Therefore, both the physical and chemical properties of biochar influence the heavy metal ion adsorption performance. Herein, PBC 600 was selected to implement further MnO_2 modification work.

Effect of different MBCs on Sb(III) adsorption

As presented in Fig. 2b, MBC samples with larger amounts of MnO_2 had high sorption capacities. The sorption capacities of 1/50MBC600, 1/30MBC600, and 1/20MBC600 were 13.48 $mg{\cdot}g^{-1}$, 22.68 $mg{\cdot}g^{-1}$ and 34.56 $mg{\cdot}g^{-1}$, respectively. It is noteworthy that the sorption capacity of all MnO_2-modified biochar samples (1/50MBC600, 1/30MBC600, and 1/20MBC600) exceeded that of PBC600 as expected. The improved Sb(III) removal by MBC600 was ascribed to the higher porosity (i.e. specific surface area and mesoporosity, Table 1) and the presence of MnO_2 (Cuong et al. 2021). More specifically, the removal capacity of Sb(III) by 1/20MBC600 was 9.6 times higher than that of PBC600. The increase in MnO_2-coated material increased the number of adsorption sites of the biochar sample, thus increasing the contact between the biochar and Sb and allowing Sb in aqueous solution to more easily adsorb onto MBC600 (Jia et al. 2020). The corresponding concentrations of Sb(III) and Sb(V) over time were measured and are presented in Fig. S3a b.

Effect of initial Sb(III) concentration

The effects of the initial Sb(III) concentration (C_0: 50 ~ 200 $mg{\cdot}L^{-1}$) on adsorption were evaluated while maintaining an initial pH of 4 and adsorbent dosage of 0.5 $g{\cdot}L^{-1}$ at 25 °C. The Sb(III) removal efficiencies for two types of biochar are shown in Fig. 2c, and the sorption capacity of

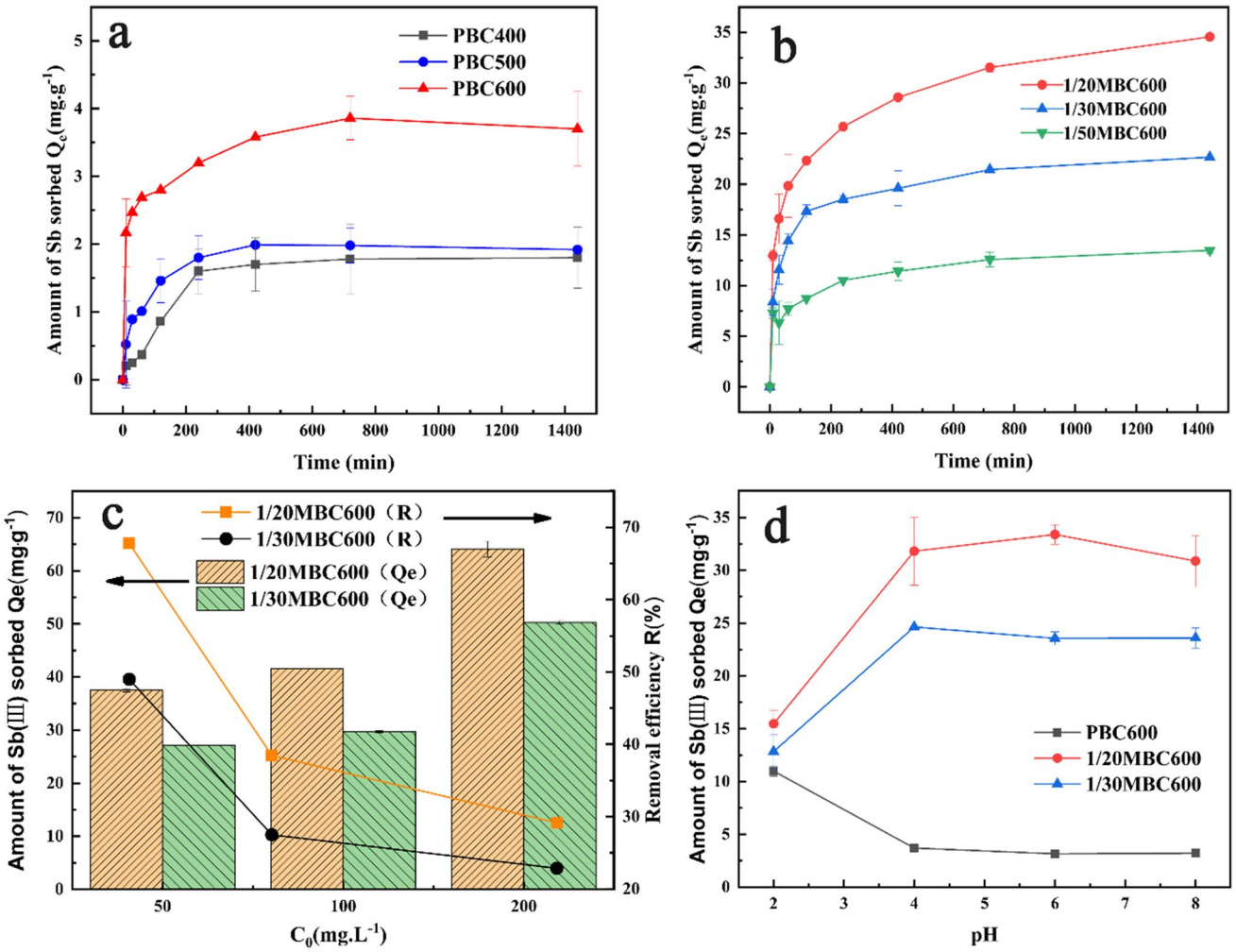

Fig. 2 Effect of (**a**) different pyrolysis temperature biochar samples and (**b**) different MnO_2-modified biochar (MBC) on Sb(III) adsorption. (**c**) Effects of different initial concentrations on the adsorption of Sb(III) by MBC and (**d**) different initial pH on the adsorption of Sb(III) by MBC and PBC600

biochar increased as the C_0 increased. Furthermore, for both types of biochar samples, the Sb(III) removal efficiencies decreased with increasing initial Sb(III) concentrations, whereas the adsorption capacities increased rapidly (Jin et al. 2021). Specifically, the maximum adsorption capacity of 1/20MBC600 reached 64.12 $mg{\cdot}g^{-1}$ when C_0 was 200 $mg{\cdot}L^{-1}$. The availability of sufficient adsorption sites allowed the material to effectively remove Sb at lower concentrations, but when C_0 was higher than 100 $mg{\cdot}L^{-1}$, the previously unoccupied binding sites in the biochar slowly became saturated or even exhausted, causing the adsorption capacity curve to taper off until the system reached equilibrium. Taking both the removal efficiency and adsorption capacity into consideration, the most suitable initial Sb(III) concentration was 100 $mg{\cdot}L^{-1}$ for all biochar samples.

1/20MBC600 was the most promising sample and showed the greatest adsorption capacity. The maximum adsorption capacity of 1/20MBC was compared with several studies published previously. Among various kinds of adsorbents, our modified method has the advantages of requiring less raw material, low cost, moderate conditions (temperature, neutral pH value), and simplicity of operation. Thus, our MBC is more feasible for large-scale implementation compared with other materials. Given the ideal costs, sources, convenience, and benefits, we found that 1/20MBC600 had the best practical performance (Table 2).

Effect of initial pH

pH is one of the key factors that affect heavy metal adsorption onto biochar. Herein, the influence of solution pH on Sb(III) adsorption by PBC600, 1/30MBC600, and 1/20MBC600 were determined in a pH range of 2 to 8. The results are described

in Fig. 2d. In general, pH had little effect on the adsorption of Sb(III) onto PBC600 and MBC600, and the capacities of these three biochar samples were relatively stable under pH conditions ranging from 4 to 8. This is consistent with studies by Cui et al., 2017) and Vithanage et al., 2015). For PBC600, the result we obtained is consistent with the work of Cui et al. (2017), with the capacity being the highest when the pH value was 2 and stable at pH values from 4 to 8. For 1/30MBC600 and 1/20MBC600, capacities were markedly diminished at a pH of 2, which is similar to the findings of Wan et al., 2020). The speciation of Sb(III) is dominated by $Sb(OH)_3$ at pH values ranging from 2 to 12 and $Sb(OH)_4^-$ when pH > 12. We speculated that this is why the capacity remained stable. As Sb(III) may be oxidised into Sb(V), Sb(III) and Sb(V) were measured and are presented in Fig. S3c d . The concentration of Sb(III) was lower and the concentration of Sb(V) was higher for both 1/30MBC600 and 1/20MBC600 at a pH of 2. This may be due to dissolved Mn^{4+} and Mn^{3+} oxidising Sb(III) to Sb(V) in the strongly acidic solution (Herath et al. 2017). The oxidation of Sb(III) by Mn^{4+} and Mn^{3+} both in solution and on biochar surfaces after sorption could result in desorption, as the resultant Sb(V) has a much lower affinity to biochar compared to Sb(III) (Jia et al. 2020; Vithanage et al. 2015). Furthermore, the decrease in the quantity of Mn in biochar would also result in a decline in the number of active sites. Hence, MBC600 possesses a very strong capacity to oxidise Sb(III) in solution and is thus beneficial for reducing the toxicity of trivalent antimony.

Sb(III) oxidation

Figure 2b and Fig. S3 are examples that demonstrate several pieces of information. For 1/30MBC600 and 1/20MBC600, it is at a pH of 2 that the concentration on Sb(III) declined drastically and Sb(V) rapidly peaked and then stabilised. In the early stage, Sb(III) was oxidised to Sb(V) and then adsorbed into MBC600. As time went on, adsorption reached saturation and MBC600 refused to adsorb Sb(V), contributing to higher Sb(V) concentration in the solution. Overall, pH had little effect on the adsorption of Sb(III) in the range of 4 to 8. The Sb(III) oxidation can be the result of: (1) the redox reaction between Mn^{4+} or Mn^{3+} dissolved in solution and Sb(III) in the solution, (2) Sb(III) being oxidised to Sb(V) by oxygen, and (3) the oxidation of adsorbed Sb(III) on the biochar surface to Sb(V) by MnO_x.

Adsorption kinetics and isotherm

The mechanism governing adsorption processes and solute distribution at the solid–liquid interface can be elucidated by different adsorption kinetic models. Herein, the adsorption kinetic data relating to Sb(III) adsorption by PBC600, 1/30MBC600, and 1/20MBC600 were fitted using pseudo-first-order and pseudo-second-order equations. The kinetic curves and relevant kinetic parameters of these three biochar samples are presented in Fig. 3a and Table 3, respectively. The effects of contact time on Sb(III) adsorption are displayed in Fig. 3, which indicates that the adsorption of Sb(III) on the three types of biochar samples occurred in two stages (Jin et al. 2021). First, at time 0–240 min, the Sb(III) adsorption process was rapid and close to the adsorption equilibrium, and then the adsorption capacity gradually reached a plateau. The initial rapid increase in adsorption can be attributed to the large number of active sites on the biochar surfaces and the sufficient amount of Sb(III). As the adsorption process went on, fewer active sites remained and adsorption capacity reached a peak. The adsorption kinetics parameters of these three biochar samples are illustrated in Table 3. The pseudo-second-order fit had a

Table 2 Adsorption capacities of Sb(III) in aqueous solution on various adsorbents

Adsorbent	Sb (III) ($mg.g^{-1}$)	Reference
Mn-coated biochar	0.94	(Jia et al. 2020)
Canna indica derived biochar	16.10	(Cui et al. 2017)
Stover-derived biochar	4.63	(Vithanage et al. 2015)
Mercapto functionalised silica-supported organic–inorganic hybrid sorbent	108.80	(Fan et al. 2016)
$MnFe_2O_4$–biochar	237.53	(Wang et al. 2018)
Magnesium oxide	140.10	(Xu et al. 2020)
MO-L-Biochar	248.0	(Wan et al. 2020)
CTAB/$MnFe_2O_4$/MnO_2	321.03	(Yao et al. 2020)
Fe-loaded biochar	48.78	(Calugaru et al. 2019)
rGO-Fe/Ni composite	2.48	(Lin et al. 2021)
biochar-supported magnetic UiO-66-2COOH	56.49	(Zhu et al. 2021)
Nano-zero-valent iron sludge-based biochar	160.40	(Wei et al. 2020)
1/20MBC600	64.12	this study

higher R^2 (>0.9) value than the pseudo-first-order model not only for PBC600 but also for 1/30MBC600 and 1/20MBC600, and the predicted maximum adsorption capacity for Sb(III) was close to that observed in experimental data. As is well known, the pseudo-second-order equation matches chemical adsorption, indicating that this adsorption is a complicated process mainly affected by the chemical interactions between Sb and MBC600, such as complexation and other reactions, as well as the physical adsorption of Sb at the active sites of the biochar (Jia et al. 2020). Therefore, the results obtained suggested that the adsorption of Sb(III) on the three types of biochar samples studied was governed predominantly by chemical rather than physical processes (Liu et al. 2021b).

Adsorption isotherms represent the equilibrium relationship between the solution concentration and the adsorption capacity at a constant temperature (Jiang et al. 2017). Langmuir and Freundlich models at two different temperatures (25 °C and 35 °C) were applied to determine the impact of temperature on Sb(III) removal onto MBC. The Langmuir model assumes monolayer adsorption between solid and gas phases, while the Freundlich equation is a semi-empirical equation that is related to multilayer adsorption (Zhu et al. 2021). The regression parameters are presented in Tab. 4. Both the Langmuir (R_L^2=0.76–0.99) and Freundlich models (R_F^2=0.85–0.99) showed convincing isotherms at two temperatures, suggesting that Sb(III) adsorption onto the MBC600 is a heterogeneous chemisorption process comprising a monolayer and multilayer adsorption (Jia et al. 2020). The R_L^2 value of the Langmuir equation is related to the affinity between adsorbate and adsorbent. The larger the R_L^2 value, the higher the affinity of the adsorbate and the adsorbent. The high value of R_L^2 observed for Sb(III) indicates that Sb(III) has a high affinity for adsorption onto MBC600. At two different temperatures, the n values of 1/30MBC600 and 1/20MBC600 for Sb(III) ranged 0.53–0.56 and 0.37–0.55, respectively, suggesting that the adsorption process was likely a chemical process (Zhu et al. 2021). The result obtained from adsorption isotherms is in accordance with the adsorption kinetics data.

Adsorption mechanisms

FT-IR spectrum analysis

Biochar contains abundant functional groups, which can provide reaction or interaction sites on the material surface for

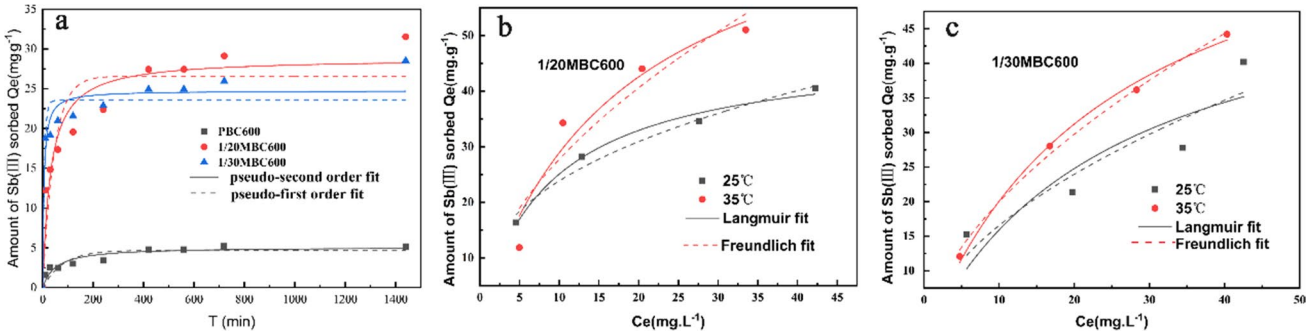

Fig. 3 Adsorption kinetics of Sb(III) onto the PBC600 and MBCs (**a**) and adsorption isotherms of Sb(III) (**b** and **c**)

Table 3 Parameters of the two kinds of kinetic model for PBC600, 1/30MBC600, and 1/20MBC600

Adsorbent	The pseudo-first-order model			The pseudo-second-order model		
	q_e/mg.g^{-1}	K_1	R^2	q_e/mg.g^{-1}	K_2	R^2
PBC600	4.70	0.01	0.83	5.10	0.004	0.90
1/20MBC600	26.59	0.03	0.83	28.84	0.001	0.92
1/30MBC600	23.55	0.15	0.90	24.76	0.008	0.93

Tab 4 Parameters of the two kinds of adsorption isotherms for PBC600, 1/30MBC600, and 1/20MBC600

Adsorbent		Langmuir			Freundlich		
		q_m/mg.g^{-1}	b	R_L^2	n	K_F	R_F^2
35℃	1/20MBC600	80.61	0.06	0.94	0.55	7.83	0.88
	1/30MBC600	70.28	0.03	0.99	0.56	5.31	0.99
25℃	1/20MBC600	55.98	0.11	0.99	0.37	10.08	0.98
	1/30MBC600	47.99	0.04	0.76	0.53	4.86	0.85

the transformation and sorption of metal ions. FT-IR spectroscopy was used to probe the surface functional groups of different biochar materials and the results for PBC600 and 1/20MBC600 before and after adsorption are provided in Fig. 4a. The peaks at 3440 cm^{-1}, 2924 cm^{-1}, 1441 cm^{-1}, and 879 cm^{-1} were detected on all the samples, which corresponded to –OH, C–H, CO_3^{2-}, and CO_3^{2-}, respectively. This suggests that these functional groups exist on all four types of materials (Jin et al. 2021). Interestingly, there was a new peak at 575 cm^{-1} that appeared on PBC600 after modification with Mn; this was caused by Mn–O bonds and weakened after Sb adsorption, providing further evidence that Mn–O bonds on the 1/20MBC600 took part in the interaction between Sb and biochar (Cuong et al. 2021). Furthermore, there were also differences in the strong characteristic peaks at 1441 cm^{-1} and 879 cm^{-1} relating to the stretching and bending motions of CO_3^{2-}. These peaks had the greatest intensity in the PBC600 spectrum and were also more intense before adsorption than after (PBC600 > PBC600-Sb, 1/20MBC600 > 1/20MBC600-Sb) (Zhang et al. 2021a). This phenomenon was probably caused by the dissolution of CO_3^{2-}.

XRD analysis

The characteristics of the crystal structures and phase compositions of PBC600 and 1/20MBC600 before and after Sb(III) adsorption were investigated by XRD analysis. As shown in Fig. 4b, there were no obvious manganese dioxide peaks present, which implied poorly crystalline forms of manganese oxides. The main crystal of PBC600 and 1/20 MBC600 was $CaCO_3$, further validating their poor crystallinity both before and after Sb(III) adsorption (Shen et al. 2020). After Sb(III) adsorption, the diffraction peak intensities of the $CaCO_3$ crystal in PBC600 and 1/20 MBC600 decreased, likely due to the dissolution of $CaCO_3$ (Zhang et al. 2020b). However, the Sb crystal could not be detected in XRD patterns. This phenomenon may be attributed to the low crystal content of Sb adsorbed on the surface of biochar. Generally, it is difficult to detect crystals that comprise less than 5% of the total, and the higher strength of $CaCO_3$ crystals involved in PBC600 and 1/20 MBC600 would conceal the diffraction peaks of other crystals, thus influencing Sb detection. Similar biochar samples containing abundant $CaCO_3$ were studied by Lian et al., 2020) and Zhang et al. (2021a). The result obtained from XRD is in accordance with the FT-IR results.

XPS spectra analysis

High-resolution XPS spectra of Sb3d3/2 and Mn2p3/2 for 1/20MBC600 before and after Sb(III) adsorption are presented in Fig. 5. As evident from Fig. 5a and c, while Sb was not detected on 1/20MBC600 before adsorption, it was detected after adsorption, affirming that Sb was adsorbed on Mn-modified biochar (Jia et al. 2020). The adsorbed Sb on 1/20MBC600 included 55.98% in the Sb(III) state (at 539.9 eV) and 44.02% in the Sb(V) state (at 540.5 eV). This suggests that some of the Sb(III) was oxidised to Sb(V) in the process of adsorption and that Sb(V) was combined with 1/20MBC600 by inner-sphere complexation (Wan et al. 2020). High-resolution spectra of Mn2p3/2 for 1/20MBC600 before and after adsorption are presented in Fig. 5b and d. Both before and after adsorption, satellite peaks in the Mn2p3/2 spectra were detected. The binding energies of Mn2p3/2 at around 641.5 eV, 642.7 eV, and 643.9 eV were assigned to Mn(II), Mn(III), and Mn(IV), respectively. The respective peak area ratios of Mn(II), Mn(III), and Mn(IV) were 12.10%, 45.94%, and 41.96% before adsorption. However, after adsorption, these changed to 41.12%, 35.56%, and 25.32%, respectively. After Sb(III) adsorption, the proportion of Mn(IV) and Mn(III) on 1/20MBC600 surface

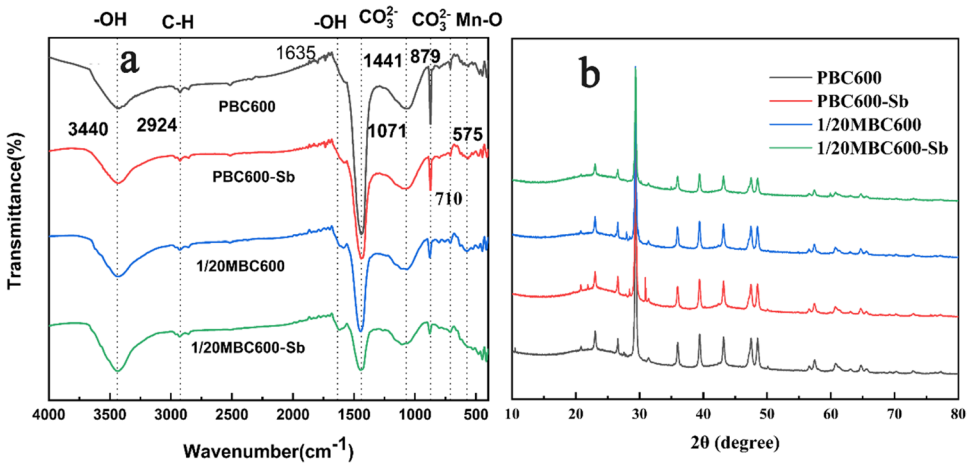

Fig. 4 **a** FT-IR and **b** XRD patterns of PBC600 and 1/20MBC600 before and after Sb(III) adsorption

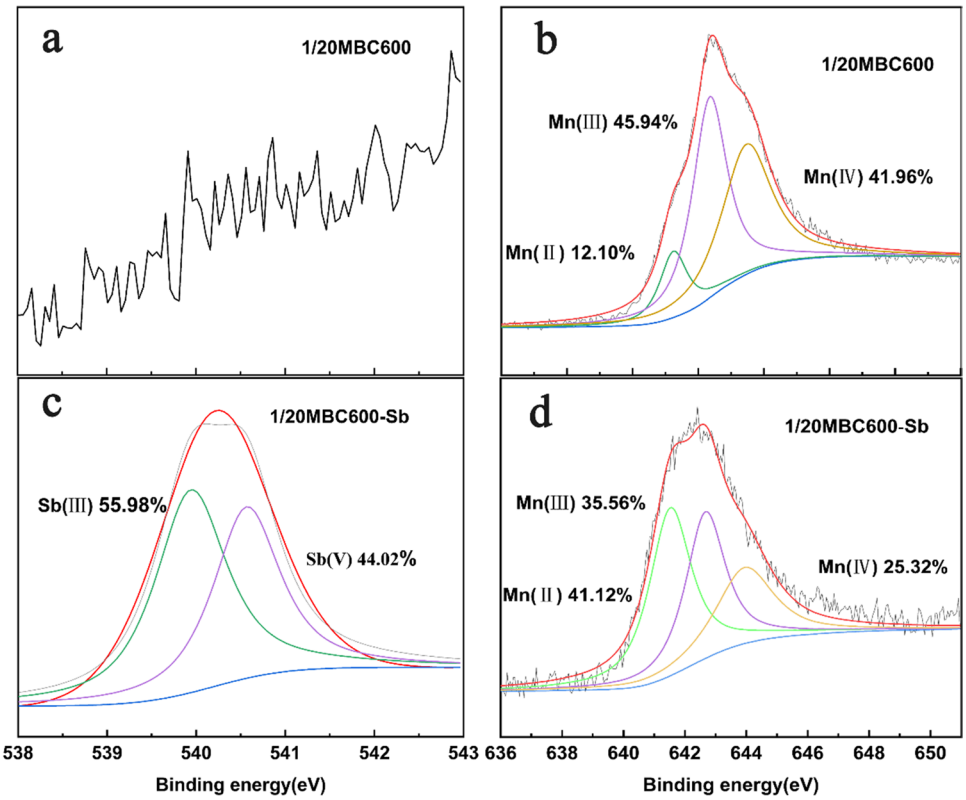

Fig. 5 Sb3d3/2 spectra for 1/20MBC600 before (**a**) and after (**c**) Sb(III) adsorption, Mn2p3/2 spectra for 1/20MBC600 before (**b**) and after (**d**) Sb(III) adsorption

diminished significantly. On the contrary, the proportion of Mn(II) increased to 41.12%. Therefore, a reasonable inference was proposed: Mn(IV) and Mn(III) on MBC were converted to Mn(II) by a redox reaction between Mn(IV), Mn(III), and Sb(III) (Wan et al. 2020). Interestingly, the Mn peak area decreased by 46.66% after adsorption of Sb(III)

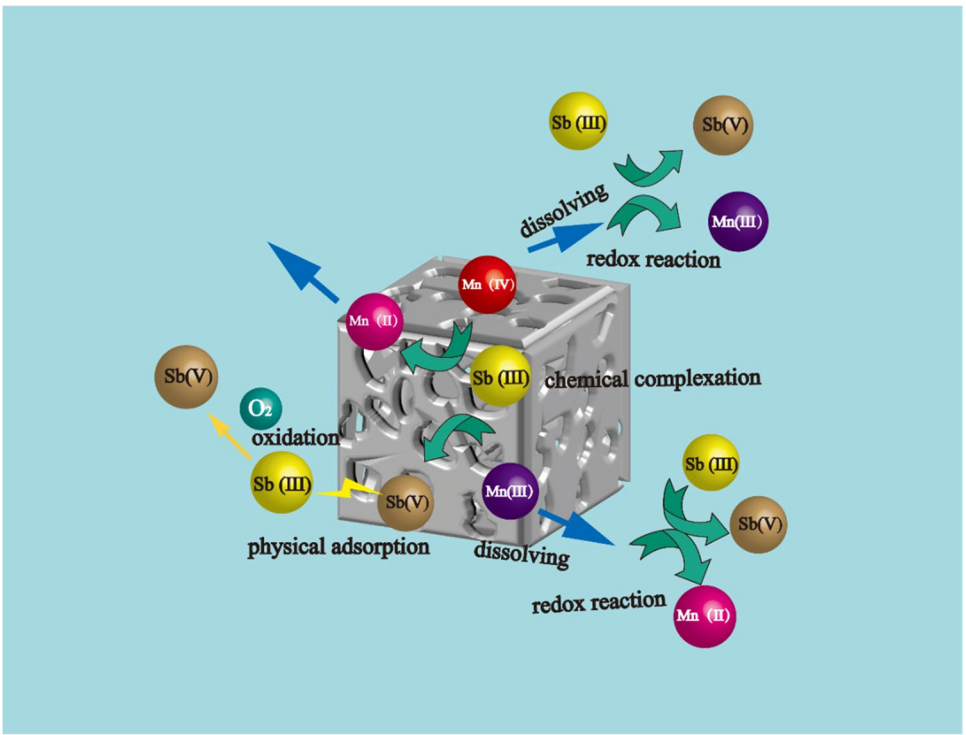

Fig. 6 Schematic diagram of Sb(III) adsorption onto the MBC

by 1/20MBC600, indicating that approximately half of the Mn was dissolved into solution in the process of adsorption, which is consistent with the work of Jia et al.(2020). The XPS analysis confirmed that MnO_x was involved in the reaction of Sb(III) with MBC600 (Fig. 6).

Conclusions

In this paper, a low-cost and high-efficiency MnO_2-modified biochar was synthesised, showing superior adsorption capacity for Sb(III) compared to other biochar samples reported in the literature. After modification with MnO_2, the capacity of biochar derived from discarded mushroom-stick showed obvious improvements, not only in maintaining stable and superior adsorption performance in a pH range of 4 to 8 but also in having a stronger ability to oxidise Sb(III). Therefore, this material has a strong potential to counter Sb(III) toxicity. The adsorption mechanisms of Sb onto MBC600 involved physical adsorption and chemical complexation reactions which form monodentate mononuclear and edge-sharing complexes. These results suggest that MBC600 is an excellent adsorbent that can potentially be used for antimony removal in water bodies. Thus, MnO_2-modified biochar derived from discarded mushroom-stick is an excellent adsorbent with great promise for future application.

Supplementary Information The online version contains supplementary material available at https://doi.org/10.1007/s11356-021-18276-7.

Acknowledgements This research has been supported by the Science and Technology Planning Project of Guizhou Province (Grant No. [2019]2864), Fund for Newly-enrolled Talent of Guizhou University (Grant 48 No. 2018(33)), and National Key R&D Program of China (Grant No. 2018YFC1801705).

Authors' contributions All authors contributed to the study conception and design. The first draft of the manuscript and the drawing of the diagram were completed by **Wenjian Mao** and all authors commented on previous versions of the manuscript. Manuscript writing guidance and the first draft revision were completed by the corresponding author **Jian Zhu**, **Pan Wu,** and **Kaidi Lai**. Experimental operation, data collation, and sample collection were performed by **Yuqin Zhang**, **Lisha Dong**, **Xufeng Qian,** and **Yutao Zhang**. All authors read and approved the final manuscript.

Funding This research has been supported by the Science and Technology Planning Project of Guizhou Province (Grant No. [2019]2864), Fund for Newly-enrolled Talent of Guizhou University (Grant 48 No. 2018(33)), and National Key R&D Program of China (Grant No. 2018YFC1801705).

National Key R&D Program of China,No.2018YFC1801705,Jian Zhu,Science and Technology Planning Project of Guizhou Province,No. [2019]2864,Jian Zhu,Fund for Newly-enrolled Talent of Guizhou University,No. [2018]33,Jian Zhu

Availability of data and materials The authors declare that [the/all other] data supporting the findings of this study are available within the article [and its supplementary information files].

Declarations

Ethics approval and consent to participate Not applicable.

Consent for publication All authors agreed to publish this research (including any individual details, images, or videos) in *Environmental Science and Pollution Research.*

Competing interests The authors declare that they have no known competing financial interests or personal relationships that could have appeared to influence the work reported in this paper "Manganese oxide-modified biochar derived from discarded mushroom-stick for the removal of Sb(III) from aqueous solution".

References

Calugaru IL, Neculita CM, Genty T, Zagury GJ (2019) Removal efficiency of As(V) and Sb(III) in contaminated neutral drainage by Fe-loaded biochar. Environ Sci Pollut Res 26:9322–9332

Castanho NRCM, de Oliveira RA, Batista BL, Freire BM, Lange C, Lopes AM, Jozala AF, Grotto D (2021) Comparative Study on Lead and Copper Biosorption Using Three Bioproducts from Edible Mushrooms Residues. J Fungi 7:441–492

Chen G, Yu H, Lin F, Zhang Z, Yan B, Song Y (2020) Utilization of edible fungi residues towards synthesis of high-performance porous carbon for effective sorption of Cl-VOCs. Sci Total Environ 727:138475

Cheng J, Gu J-J, Tao W, Wang P, Liu L, Wang C-Y, Li Y-K, Feng X-H, Qiu G-H, Cao F-F (2019) Edible fungus slag derived nitrogen-doped hierarchical porous carbon as a high-performance adsorbent for rapid removal of organic pollutants from water. Bioresour Technol 294:122149

Costa Ferreira SL, dos Anjos JP, Assis Felix CS, da Silva Junior MM, Palacio E, Cerda V (2019) Speciation analysis of antimony in environmental samples employing atomic fluorescence spectrometry – Review. TrAC, Trends Anal Chem 110:335–343

Cui X, Ni Q, Lin Q, Khan KY, Li T, Khan MB, He Z, Yang X (2017) Simultaneous sorption and catalytic oxidation of trivalent antimony by Canna indica derived biochars. Environ Pollut 229:394–402

Cuong DV, Wu P-C, Chen L-I, Hou C-H (2021) Active MnO_2/biochar composite for efficient As(III) removal: Insight into the mechanisms of redox transformation and adsorption. Water Res 188:116495

Fan H-T, Sun W, Jiang B, Wang Q-J, Li D-W, Huang C-C, Wang K-J, Zhang Z-G, Li W-X (2016) Adsorption of antimony(III) from aqueous solution by mercapto-functionalized silica-supported organic–inorganic hybrid sorbent: Mechanism insights. Chem Eng J 286:128–138

Gao M, Zhang Y, Gong X, Song Z, Guo Z (2018) Removal mechanism of di-n-butyl phthalate and oxytetracycline from aqueous solutions by nano-manganese dioxide modified biochar. Environ Sci Pollut Res Int 25:7796–7807

Ge X, Liu J, Song X, Wang G, Zhang H, Zhang Y, Zhao H (2016) Hierarchical iron containing γ-MnO_2 hollow microspheres: A facile one-step synthesis and effective removal of As(III) via oxidation and adsorption. Chem Eng J 301:139–148

Guo W, Zhang Z, Wang H, Qin H, Fu Z (2021) Exposure characteristics of antimony and coexisting arsenic from multi-path exposure in typical antimony mine area. J Environ Manag 289:112493
He M, Wang X, Wu F, Fu Z (2012) Antimony pollution in China. Sci Total Environ 421–422:41–50
He Y, Wang L, Chen Z, Shen B, Wei J, Zeng P, Wen X (2021) Catalytic ozonation for metoprolol and ibuprofen removal over different MnO_2 nanocrystals: Efficiency, transformation and mechanism. Sci Total Environ 785:147328
Herath I, Vithanage M, Bundschuh J (2017) Antimony as a global dilemma: Geochemistry, mobility, fate and transport. Environ Pollut 223:545–559
Herath A, Layne CA, Perez F, Hassan EIB, Pittman CU, Mlsna TE (2021) KOH-activated high surface area Douglas Fir biochar for adsorbing aqueous Cr(VI), Pb(II) and Cd(II). Chemosphere 269:128409
Hou Y, Liang Y, Hu H, Tao Y, Zhou J, Cai J (2021) Facile preparation of multi-porous biochar from lotus biomass for methyl orange removal: Kinetics, isotherms, and regeneration studies. Bioresource Technol 329:124877
Hu B, Ai Y, Jin J, Hayat T, Alsaedi A, Zhuang L, Wang X (2020) Efficient elimination of organic and inorganic pollutants by biochar and biochar-based materials. Biochar 2:47–64
Hu Q et al (2021) Biochar industry to circular economy. Sci Total Environ 757:143820
Huang W-H, Lee D-J, Huang C (2021) Modification on biochars for applications: A research update. Bioresource Technol 319:124100
Jia X, Zhou J, Liu J, Liu P, Yu L, Wen B, Feng Y (2020) The antimony sorption and transport mechanisms in removal experiment by Mn-coated biochar. Sci Total Environ 724:138158
Jiang L, Liu S, Liu Y, Zeng G, Guo Y, Yin Y, Cai X, Zhou L, Tan X, Huang X (2017) Enhanced adsorption of hexavalent chromium by a biochar derived from ramie biomass (Boehmeria nivea (L.) Gaud.) modified with beta-cyclodextrin/poly(L-glutamic acid). Environ Sci Pollut Res Int 24:23528–23537
Jin Y, Zhang M, Jin Z, Wang G, Li R, Zhang X, Liu X, Qu J, Wang H (2021) Characterization of biochars derived from various spent mushroom substrates and evaluation of their adsorption performance of Cu(II) ions from aqueous solution. Environ Res 196:110323
Kamran U, Park S-J (2020) MnO_2-decorated biochar composites of coconut shell and rice husk: An efficient lithium ions adsorption-desorption performance in aqueous media. Chemosphere 260:127500
Khan N, Chowdhary P, Gnansounou E, Chaturvedi P (2021) Biochar and environmental sustainability: Emerging trends and techno-economic perspectives. Bioresource Technol 332:125102
Kumar H, Bhardwaj K, Sharma R, Nepovimova E, Cruz-Martins N, Dhanjal DS, Singh R, Chopra C, Verma R, Abd-Elsalam KA, Tapwal A, Musilek K, Kumar D, Kuča K (2021) Potential Usage of Edible Mushrooms and Their Residues to Retrieve Valuable Supplies for Industrial Applications. Journal of Fungi 7:427–444
Leng L, Xiong Q, Yang L, Li H, Zhou Y, Zhang W, Jiang S, Li H, Huang H (2021) An overview on engineering the surface area and porosity of biochar. Sci Total Environ 763:144204
Li G, Zhao P, Zheng H, Yang L, Lu S, Peng P (2018) Research on the removal mechanism of antimony on α-MnO_2 nanorod in aqueous solution: DFT + U method. J Hazard Mater 354:8–16
Li H, Liu L, Cui J, Cui J, Wang F, Zhang F (2020) High-efficiency adsorption and regeneration of methylene blue and aniline onto activated carbon from waste edible fungus residue and its possible mechanism. RSC Adv 10:14262–14273
Li Y, Zhang M, Xu R, Lin H, Sun X, Xu F, Gao P, Kong T, Xiao E, Yang N, Sun W (2021) Arsenic and antimony co-contamination influences on soil microbial community composition and functions: Relevance to arsenic resistance and carbon, nitrogen, and sulfur cycling. Environ Int 153:106522
Lian W, Yang L, Joseph S, Shi W, Bian R, Zheng J, Li L, Shan S, Pan G (2020) Utilization of biochar produced from invasive plant species to efficiently adsorb Cd (II) and Pb (II). Bioresource Technol 317:124011
Lin Z, Weng X, Khan NI, Owens G, Chen Z (2021) Removal mechanism of Sb(III) by a hybrid rGO-Fe/Ni composite prepared by green synthesis via a one-step method. Sci Total Environ 788:147844
Liu C, Ding R, Xie F (2020) Facile Synthesis of Manganese Dioxide Nanoparticles for Efficient Removal of Aqueous As(III). J Chem Eng Data 65:3988–3997
Liu L, Liu G, Zhou J, Jin R (2021) Interaction between hexavalent chromium and biologically formed iron mineral-biochar composites: Kinetics, products and mechanisms. J Hazard Mater 405:124246
Liu Z, Wang Z, Tang S, Liu Z (2021) Fabrication, characterization and sorption properties of activated biochar from livestock manure via three different approaches. Resour Conserv Recycl 168:105254
Luo G, Han Z, Xiong J, He Y, Liao J, Wu P (2021) Heavy metal pollution and ecological risk assessment of tailings in the Qinglong Dachang antimony mine, China. Environ Sci Pollut Res Int 28:33491–33504
Nishad PA, Bhaskarapillai A (2021) Antimony, a pollutant of emerging concern: A review on industrial sources and remediation technologies. Chemosphere 277:130252
Pan X, Gu Z, Chen W, Li Q (2021) Preparation of biochar and biochar composites and their application in a Fenton-like process for wastewater decontamination: A review. Sci Total Environ 754:142104
Qi P, Wang Y, Zeng J, Sui K, Zhao J (2021) Progress in antimony capturing by superior materials: Mechanisms, properties and perspectives. Chem Eng J 419:130013
Shen Q, Wang Z, Yu Q, Cheng Y, Liu Z, Zhang T, Zhou S (2020) Removal of tetracycline from an aqueous solution using manganese dioxide modified biochar derived from Chinese herbal medicine residues. Environ Res 183:109195
Song J, He Q, Hu X, Zhang W, Wang C, Chen R, Wang H, Mosa A (2019) Highly efficient removal of Cr(VI) and Cu(II) by biochar derived from Artemisia argyi stem. Environ Sci Pollut Res Int 26:13221–13234
Thomas E, Borchard N, Sarmiento C, Atkinson R, Ladd B (2020) Key factors determining biochar sorption capacity for metal contaminants: a literature synthesis. Biochar 2:151–163
Tian S-Q, Qi J-Y, Wang Y-P, Liu Y-L, Wang L, Ma J (2021) Heterogeneous catalytic ozonation of atrazine with Mn-loaded and Fe-loaded biochar. Water Res 193:116860
Vithanage M, Rajapaksha AU, Ahmad M, Uchimiya M, Dou X, Alessi DS, Ok YS (2015) Mechanisms of antimony adsorption onto soybean stover-derived biochar in aqueous solutions. J Environ Manage 151:443–449
Wan S, Qiu L, Li Y, Sun J, Gao B, He F, Wan W (2020) Accelerated antimony and copper removal by manganese oxide embedded in biochar with enlarged pore structure. Chem Eng J 402:126021
Wang S, Gao B, Li Y, Mosa A, Zimmerman AR, Ma LQ, Harris WG, Migliaccio KW (2015) Manganese oxide-modified biochars: Preparation, characterization, and sorption of arsenate and lead. Biores Technol 181:13–17
Wang Y, Kong L, He M, Ouyang W, Lin C, Liu X (2020) Influences of Particles and Aquatic Colloids on the Oxidation of Sb(III) in Natural Water. ACS Earth and Space Chemistry 4:661–671
Wei D, Li B, Luo L, Zheng Y, Huang L, Zhang J, Yang Y, Huang H (2020) Simultaneous adsorption and oxidation of antimonite onto nano zero-valent iron sludge-based biochar: Indispensable role

of reactive oxygen species and redox-active moieties. J Hazard Mater 391:122057
Xu S, Zhong Z, Liu W, Deng H, Lin Z (2020) Removal of Sb(III) from wastewater by magnesium oxide and the related mechanisms. Environ Res 186:109489
Yang R, Fan Y, Ye R, Tang Y, Cao X, Yin Z, Zeng Z (2021) MnO_2-Based Materials for Environmental Applications. Adv Mater 33:2004862
Yao X, Ji L, Guo J, Ge S, Lu W, Chen Y, Cai L, Wang Y, Song W (2020) An abundant porous biochar material derived from wakame (Undaria pinnatifida) with high adsorption performance for three organic dyes. Bioresource Technol 318:124082
Zhang H, Xu F, Xue J, Chen S, Wang J, Yang Y (2020a) Enhanced removal of heavy metal ions from aqueous solution using manganese dioxide-loaded biochar: Behavior and mechanism. Sci Rep 10:6067
Zhang J, Hu X, Yan J, Long L, Xue Y (2020b) Crayfish shell biochar modified with magnesium chloride and its effect on lead removal in aqueous solution. Environ Sci Pollut Res 27:9582–9588
Zhang D, Zhang K, Hu X, He Q, Yan J, Xue Y (2021) Cadmium removal by $MgCl_2$ modified biochar derived from crayfish shell waste: Batch adsorption, response surface analysis and fixed bed filtration. J Hazard Mater 408:124860
Zhang X, Xie N, Guo Y, Niu D, Sun H-b, Yang Y (2021) Insights into adsorptive removal of antimony contaminants: Functional materials, evaluation and prospective. J Hazard Mater 418:126345
Zhu G, Lin J, Yuan Q, Wang X, Zhao Z, Hursthouse AS, Wang Z, Li Q (2021) A biochar supported magnetic metal organic framework for the removal of trivalent antimony. Chemosphere 282:131068
Zou H, Zhao J, He F, Zhong Z, Huang J, Zheng Y, Zhang Y, Yang Y, Yu F, Bashir MA, Gao B (2021) Ball milling biochar iron oxide composites for the removal of chromium (Cr(VI)) from water: Performance and mechanisms. J Hazard Mater 413:125252